ACS Catalysis

Research Article

pubs.acs.org/acscatalysis

Pd_2Ga-Based Colloids as Highly Active Catalysts for the Hydrogenation of CO_2 to Methanol

Andrés García-Trenco,[†,§] Edward R. White,[†] Anna Regoutz,[‡] David J. Payne,*[,‡] Milo S. P. Shaffer,*[,†] and Charlotte K. Williams*[,†,§]

[†]Department of Chemistry and [‡]Department of Materials, Imperial College London, London, U.K. SW7 2AZ

[§]Department of Chemistry, University of Oxford, Chemistry Research Laboratory, 12 Mansfield Road, Oxford, U.K. OX1 3TA

Supporting Information

ABSTRACT: Colloidal Pd_2Ga-based catalysts are shown to catalyze efficiently the hydrogenation of CO_2 to methanol. The catalysts are produced by the simple thermal decomposition of Pd(II) acetate in the presence of Ga(III) stearate, which leads to Pd^0 nanoparticles (ca. 3 nm), and the subsequent Pd-mediated reduction of Ga(III) species at temperatures ranging from 210 to 290 °C. The resulting colloidal Pd_2Ga-based catalysts are applied in the liquid-phase hydrogenation of carbon dioxide to methanol at high pressure (50 bar). The intrinsic activity is around 2-fold higher than that obtained for the commercial Cu-ZnO-Al_2O_3 (60.3 and 37.2 × 10^{-9} mol_{MeOH} m^{-2} s^{-1}), respectively, and 4-fold higher on a Cu or Pd molar basis (3330 and 910 μmol $mmol_{Pd\ or\ Cu}^{-1}$ h^{-1}). Detailed characterization data (HR-TEM, STEM/EDX, XPS, and XRD) indicate that the catalyst contains Pd_2Ga nanoparticles, of average diameters 5−6 nm, associated with a network of amorphous Ga_2O_3 species. The proportion of this Ga_2O_3 phase can be easily tuned by adjusting the molar ratio of the Pd:Ga precursors. A good correlation was found between the intrinsic activity and the content of Ga_2O_3 surrounding the Pd_2Ga nanoparticles (XPS), suggesting that methanol is formed by a bifunctional mechanism involving both phases. The increase in the reaction temperature (190−240 °C) leads to a gradual decrease in methanol selectivity from 60 to 40%, while an optimum methanol production rate was found at 210 °C. Interestingly, unlike the conventional Cu-ZnO-Al_2O_3, which experienced approximately 50% activity loss over 25 h time on stream, the Pd_2Ga-based catalysts maintain activity over this time frame. Indeed, characterization of the Pd/Ga mixture postcatalysis revealed no ripening of the nanoparticles or changes in the phases initially present.

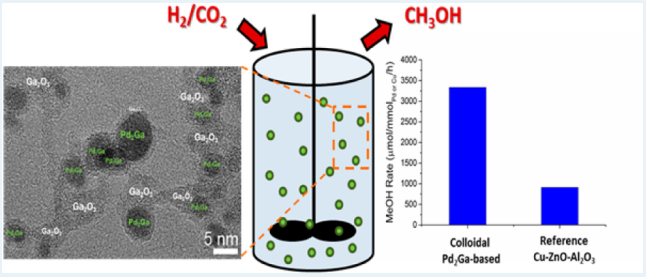

KEYWORDS: *colloidal nanoparticles, nanocatalysts, Pd_2Ga alloy, bimetallic PdGa, CO_2 hydrogenation, methanol synthesis*

1. INTRODUCTION

The hydrogenation of CO_2 to methanol, using H_2 derived from renewable or off-peak power, is a promising strategy to reduce our dependence on fossil resources.[1] The methanol produced is an important chemical feedstock but is also an attractive liquid energy carrier suitable for energy storage and transportation applications. It can be used directly as fuel or in blends with gasoline,[2] in conventional combustion engines, or for use in fuel cells.[3] Methanol is currently commercially produced on a large scale from natural gas through a syngas route. Steam methane reforming produces a mixture of CO, CO_2, and H_2 that is subsequently converted to methanol using heterogeneous Cu-ZnO-Al_2O_3 catalysts.[4] Isotopic labeling and modeling studies suggest that the methanol derives from the CO_2 in the syngas, under the typical industrial reaction conditions.[5,6] It is known that Cu-ZnO-Al_2O_3 catalysts are also active for the direct hydrogenation of CO_2 to methanol, although with only moderate activity and insufficient stability.[7,8] Over the past decade, Fischer and co-workers have pioneered the use of mixtures of colloidal Cu and ZnO nanoparticles (NPs) for the synthesis of methanol from syngas, reporting activities comparable to or slightly better than those obtained for the benchmark Cu-ZnO-Al_2O_3 heterogeneous catalysts.[9−12] This approach has also been studied and applied successfully by our group in the hydrogenation of CO_2 to methanol, as well as in the direct synthesis of DME from syngas.[13−15] Colloidal Cu and ZnO NPs exhibit high surface areas, and mixtures readily form the Cu/ZnO interface thought to be the active site for methanol synthesis.[16−18] The colloidal system allows a number of properties to be easily tuned, including catalyst composition, particle size, solubility, and surface functionality.[19] These stabilized colloidal catalysts are applied in liquid-phase reactors where the temperature gradients can be easily controlled, a feature which may be desirable to obviate the typical deactivation attributed to the poor temperature control fixed-bed technologies.[20] In fact, a commercial liquid-phase methanol synthesis process (LPMeOH) has been developed, on the basis of conventional heterogeneous catalysts used as a slurry;[20]

Received: October 13, 2016
Revised: December 2, 2016
Published: January 10, 2017

DOI: 10.1021/acscatal.6b02928
ACS Catal. 2017, 7, 1186−1196

however, a solubilized catalyst may offer improved kinetics, mass transport, and high intrinsic activity. One of the challenges in optimizing colloidal Cu/ZnO catalysts lies with controlling the interaction between the Cu NPs with their counterpart ZnO NPs to maximize the formation of active sites; individually Cu or ZnO NPs are hardly active in isolation.[16,21]

Despite the promise of the Cu/ZnO system, there is also interest in exploring other metal/oxide combinations in order to maximize performance. Heterogeneous catalysts using palladium as the active metal have shown significant promise in a range of hydrogenation and reforming reactions.[22,23] Fujitani et al. reported the first use of Pd/Ga_2O_3 catalysts for the synthesis of methanol from CO_2 and H_2,[23] obtaining activity higher than that for the Cu/ZnO system. Since then, several groups have developed Pd/Ga_2O_3 catalysts for methanol synthesis, as well as in related reactions such as methanol steam reforming or methanol decomposition.[24−38] Although there is still a lack of consensus about the role of the Pd and Ga_2O_3 phases in the reaction mechanism, it is accepted that the formation of Pd−Ga intermetallic compounds, mainly the Pd_2Ga phase, is strongly implicated in controlling catalytic activity.[24,27,30,31,34,39] Pd_2Ga NPs have mostly been studied previously in fixed-bed reactors, as heterogeneous catalysts on solid supports including $MgO/MgGa_2O_4$,[34] α-, β-, and γ-Ga_2O_3 polymorphs,[24,27] and SiO_2.[39] The syntheses typically employ the decomposition of ternary hydrotalcite-like compounds,[34] simple coprecipitation,[39] or an incipient wetness impregnation of Ga and Pd precursors.[24,27] Recently, a strong metal−support interaction was found specifically between the polar (002) Ga_2O_3 surface and supported Pd NPs, which facilitates electron transfer and the formation of $PdGa_x$.[31,32]

Given the success of the aforementioned hetereogeneous catalysts, the development of colloidal Pd_2Ga NPs catalysts for the hydrogenation of CO_2 to methanol is a desirable and as yet unexplored target. Here, a simple strategy to synthesize colloidal Pd_2Ga NPs, together with their detailed characterization and catalytic performance, is demonstrated.

2. EXPERIMENTAL SECTION

2.1. Preparation of the Catalytic Precursors. Gallium(III) stearate ($Ga(OSt)_3$) was prepared by modifying a reported method used for the synthesis of other metal stearates.[40,41] In brief, 3 equiv of stearic acid (extra pure, Fischer Scientific) was dissolved in methanol and then neutralized with a methanol solution of tetramethylammonium hydroxide (TMAOH, 98% Alfa Aesar). Afterwards, 1 equiv of $Ga(NO_3)_3$ (99.9% Alfa Aesar) dissolved in methanol was added dropwise into the neutralized solution. The white $Ga(OSt)_3$ precipitate was filtered, washed extensively with methanol, and finally dried in a vacuum oven at 50 °C. C and H contents (%), were determined by elemental analysis (Table S1 in the Supporting Information) and were in good agreement with the nominal values. FTIR spectroscopy (Figure S1 in the Supporting Information) showed the CH_2 vibrations (2850 and 2917 cm^{-1}) of the stearate chain, along with absorptions at 1449 and 1560 cm^{-1} assigned to the carboxylate symmetric and asymmetric stretches, respectively.[40,42] Pd(II) acetate ($Pd(OAc)_2$) was obtained commercially from Acros Organics (47.5 wt % Pd). A commercial precursor to the methanol synthesis catalysts, based on the ternary $CuO\text{-}ZnO\text{-}Al_2O_3$ material, was obtained from Alfa Aesar (45776; mass composition CuO 63.5%, ZnO 25.1%, Al_2O_3 10.1%, MgO 1.3%) and ground from a pellet to a fine powder using a pestle and mortar.

2.2. Characterization Techniques. Fourier transform infrared (FTIR) spectroscopy was performed with a PerkinElmer Spectrum 100 Fourier Transform IR spectrometer using a deuterated triglycine sulfate (DTGS) detector and an attenuated total reflection (ATR) accessory. Elemental analysis (EA) was carried out using a Carlo Erba Flash 2000 Elemental Analyzer. Thermogravimetric analysis (TGA) was conducted using a PerkinElmer Pyris 1 TGA instrument under N_2 flow from 100 to 700 °C, at a heating rate of 10 °C min^{-1}.

Powder X-ray diffraction (XRD) was carried out using an X'pert Pro MPD diffractometer (PANalytical BV) operating at 40 kV and 40 mA, using nickel-filtered Cu K_α radiation (λ = 0.1542 nm). To prevent contact with air during the measurements, the samples were covered by a polyimide film tape (Agar Scientific). The average crystallite size of Pd(0), Cu(0), and Pd_2Ga particles were determined by applying the Scherrer equation (shape factor of 0.9) to the most intense and not overlapped reflections at 39.9 (111), 43.5 (111), and 44.8° (020), respectively.

Transmission electron microscopy (TEM) samples were prepared by drop-casting a toluene solution onto a 300 mesh Au holey-carbon grid with an ultrathin 3 nm carbon film (Agar Scientific). Annular dark field scanning TEM (ADF-STEM) and energy dispersive X-ray (EDX) mapping were performed with a JEOL JEM 2100F scanning transmission electron microscope operated at 200 kV and equipped with an Oxford X-Max 80 SDD EDX detector. High-resolution TEM (HR-TEM) images were obtained with an aberration-corrected FEI Titan instrument operated at 300 kV. For HR-TEM imaging, samples were loaded and sealed into a Gatan Environmental Holder, under a nitrogen atmosphere in a glovebox, preventing any atmospheric exposure that might lead to inadvertent sample oxidation during transfer to the microscope. The average NP sizes were determined using HR-TEM and ADF-STEM by measuring approximately 200 NPs for each sample.

The surface of the samples was characterized using X-ray photoelectron spectroscopy (XPS). The spectra were recorded on a Thermo Scientific K-Alpha+ X-ray photoelectron spectrometer system operating at 2×10^{-9} mbar base pressure. This system incorporates a monochromated, microfocused Al K_α X-ray source ($h\nu$ = 1486.6 eV) and a 180° double-focusing hemispherical analyzer with a 2D detector. The X-ray source was operated at 6 mA emission current and 12 kV anode bias, and a flood gun was used to minimize sample charging. A small shift in binding energy (BE) caused by charging was observed for the sample PdGa290/3:1, and all spectra relating to this sample were corrected by a shift of −250 meV. Samples were mounted using conductive carbon tape and transferred to the spectrometer using a special glovebox module which prevented any exposure to air. Data were collected at 20 eV pass energy for both core level (Pd 3*d*, Ga $2p_{3/2}$, and Ga 3*d*) and valence band spectra using an X-ray spot size of 400 μm^2. All data were analyzed using the Avantage software package. For the calculation of the inelastic electron mean free path (IMFP), following the Tanuma, Powell, and Penn (TPP-2M) method, the QUASES software package was used.[43]

Pd/Ga pre- and postcatalysis samples analyzed by XRD, XPS, and TEM were prepared using typical air-sensitive techniques, in order to prevent any air exposure. As such, the samples were withdrawn from the reactor to a Schlenk tube, under a N_2 atmosphere, via a cannula with a high flow rate of N_2 (400 mL min^{-1}), washed several times with dry toluene (distilled from sodium and degassed by performing at least three freeze−

DOI: 10.1021/acscatal.6b02928
ACS Catal. 2017, 7, 1186−1196

Scheme 1. Representation of the Formation of Pd_2Ga Nanoparticles from $Ga(OSt)_3$ and $Pd(OAc)_2$ Precursors, using the Applied Synthesis Method[a]

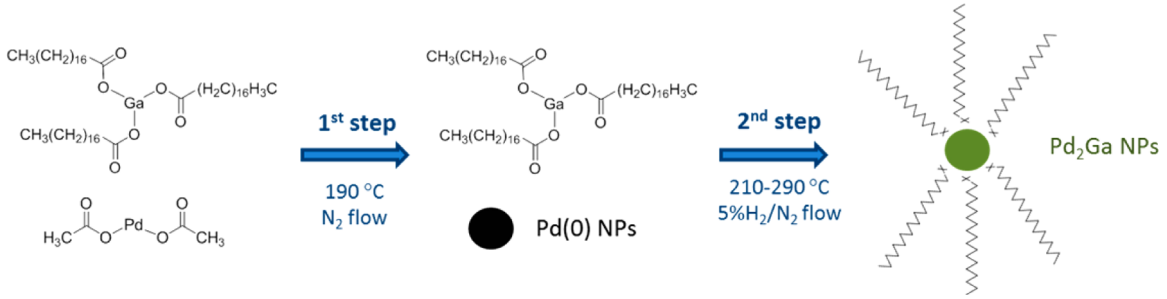

[a]X denotes an O^-/OH or CO_2^-/CO_2H terminal group.

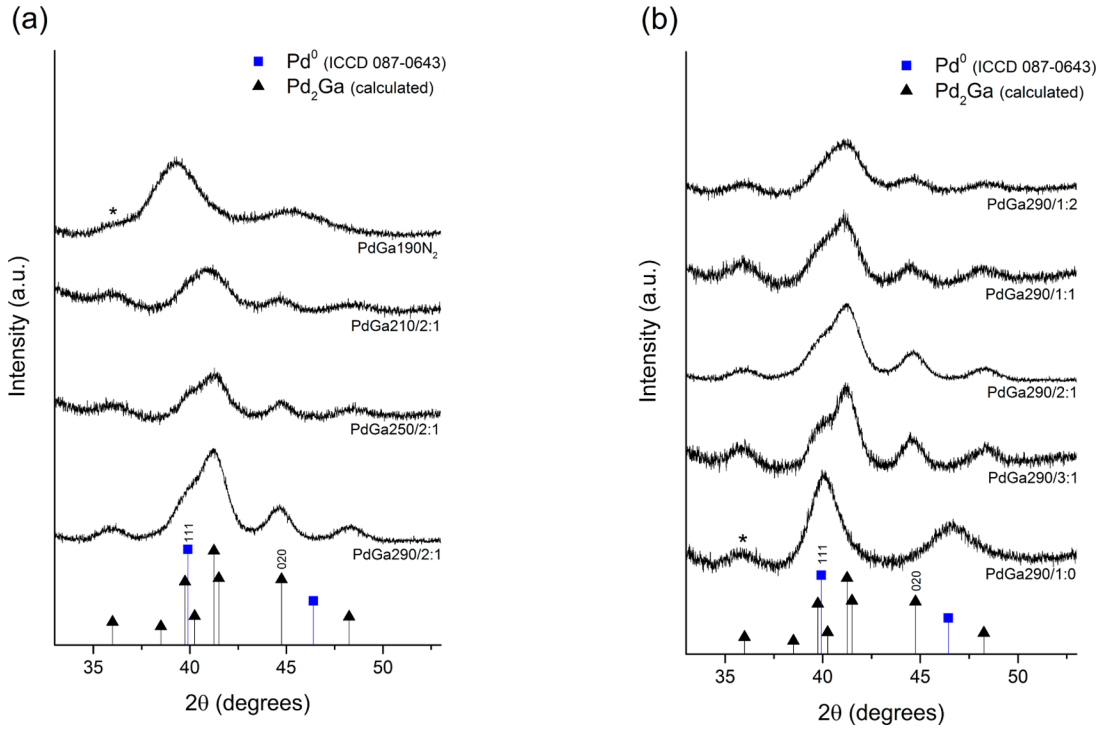

Figure 1. XRD spectra for the Pd/Ga samples (a) at different stages in the preparation and reduction temperatures and (b) prepared with different Pd/Ga composition. Asterisks denote diffraction from the polyimide film tape used to prevent the air exposure of the samples.

pump−thaw cycles, O_2 <5 ppm), and subsequently dried under vacuum (10^{-2} Pa).

2.3. Synthesis of the Pd/Ga Colloids and Catalytic Experiments. The synthesis and reaction tests were performed in a 300 mL continuous flow stirred-tank reactor (CSTR; Parr), with mechanical stirring at 1500 rpm and with vertical baffles to ensure the homogeneous mixing of the liquid and gas phases. Squalane (16 ppm of water, by Karl Fischer titration) was used as the solvent, as it exhibits a high boiling point and good gas solubility of the feed gases; it has already been reported to be an excellent solvent for the liquid-phase methanol synthesis and is widely used.[9,44] In a typical preparation procedure, the required amounts of $Pd(OAc)_2$ and $Ga(OSt)_3$ were suspended in 100 mL of squalane (3.18 $mmol_{Pd+Ga}$ L^{-1}), and the mixture was degassed with N_2 (400 mL min^{-1}) for 30 min. Then, the temperature was increased to 190 °C (6 °C min^{-1}), and after 1 h under N_2 flow (400 mL min^{-1}), the reactor was cooled to 100 °C. The resulting sample, prepared with a Pd:Ga molar ratio of 2:1, is labeled as $PdGa190N_2$. In the second preparation step, the reduction was performed by passing a 200 mL min^{-1} stream of 5% H_2/N_2 at 0.5 MPa and 210, 250, or 290 °C (3 °C min^{-1}) for 2 h. The Pd/Ga colloids are labeled as PdGa*x*/*y*:*z*, where *x* is the reduction temperature and *y*:*z* the Pd:Ga molar ratio used.

In order to perform the methanol synthesis run, the prepared Pd/Ga colloid (still in the CSTR) was submitted to the methanol synthesis conditions, which were 5.0 MPa, 210 °C, GHSV = 18.9 L $mmol_{Pd+Ga}^{-1}$ h^{-1} of a gas mixture comprising 96 vol % (75% H_2/25% CO_2), and 4 vol % Ar (used as internal standard for GC analysis) for 15 h.

The benchmark commercial Cu-ZnO-Al_2O_3 catalyst was tested as a reference material. The choice of catalyst loading was dictated by normalization considerations, making sure that the total amount of metals (Cu, Zn, Al, Mg) in moles was the same as that in the Pd/Ga colloids (3.18 $mmol_{metal}$ L^{-1}, GHSV = 18.9 L $mmol_{metal}^{-1}$ h^{-1}).[39] Before any catalysis experiments were conducted, the reference catalyst was activated using a diluted H_2 stream (5 vol % H_2/N_2) at 0.45 MPa and 240 °C

DOI: 10.1021/acscatal.6b02928
ACS Catal. 2017, 7, 1186−1196

(ramp 2 °C min^{-1}) for 3 h, according to a standard activation protocol for the ternary Cu-ZnO-Al_2O_3 methanol synthesis catalyst in slurry reactors.[45] Finally, the catalytic run was performed under the same conditions described before.

In order to investigate the influence of the reaction temperature, the optimum Pd/Ga and the reference Cu-ZnO-Al_2O_3 catalysts were also tested at 190 and 240 °C. Due to the lower activity at 190 °C, the catalyst concentration was doubled for the corresponding runs (6.36 $mmol_{metal}$ L^{-1}, GHSV = 9.5 L $mmol_{metal}^{-1}$ h^{-1}).

The reaction products and unreacted material were monitored by an online gas chromatograph (Bruker 450-GC), equipped with a thermal conductivity detector (TCD), for the quantification of CO, CO_2, and Ar, and a flame ionization detector (FID), for the quantification of MeOH and other oxygenates or hydrocarbons (if produced). To avoid any product condensation during the experiments, the lines from the reactor to the injection port of the GC were heated to 180 °C. The catalytic results were presented once the pseudosteady state was attained, typically after ca. 7 h time on stream. No deactivation was observed for the colloidal Pd/Ga catalyst for the 15 h runs. In contrast, the peak activity is given for the reference Cu-ZnO-Al_2O_3, which exhibited a distinct loss in activity with time. All experiments were conducted under differential reaction conditions, with CO_2 conversions always below 2%. Under the reaction conditions employed, the calculated CO_2 conversions at the thermodynamic limit (Aspen plus v 8.8 software), considering the methanol synthesis and the side reverse water-gas shift reaction, were 36.9, 31.8, and 26.4% at 190, 210, and 240 °C, respectively. In this study, all catalytic experiments were performed in the kinetically controlled regime. Selectivities are given on a carbon basis.

3. RESULTS AND DISCUSSION

3.1. Formation of the Colloidal Pd_2Ga-Based Catalysts. The colloidal catalysts were prepared by a two-step procedure whereby first the thermal decomposition of palladium acetate ($Pd(OAc)_2$) precursor was achieved, at 190 °C in squalane, and subsequently the colloid was reduced using a dilute hydrogen flow, at a selected temperature (Scheme 1). The first step involving the thermal decomposition reaction was monitored by TGA-MS (Figures S2 and S3 in the Supporting Information), which showed that heating a mixture of $Pd(OAc)_2$ and $Ga(OSt)_3$ to 190 °C, under an N_2 flow and at a Pd:Ga molar ratio of 2:1, leads to the decomposition of the $Pd(OAc)_2$ precursor with the byproducts being mostly acetic acid and CO_2. XRD confirmed that the resulting black colloid ($PdGa190N_2$) consists of Pd(0) crystallites with an average size of 2.8 nm (Figure 1a). The XRD pattern is shifted by 0.6° to lower 2θ angles in comparison to the reference Pd(0) crystalline phase, due to an expansion in the Pd−Pd interatomic distance known to occur for Pd(0) NPs of such a small size.[46] During the bulk preparation step, the acetic acid (boiling point 117 °C) byproduct evaporated, while $Ga(OSt)_3$ remained unreacted in the mixture, as confirmed (see below) by XPS analysis of the $PdGa190N_2$ sample.

In the second reaction step, the Pd/Ga mixture was submitted to a dilute H_2 flow (5%H_2/N_2, 0.5 MPa) at one of three different reduction temperatures (210, 250, and 290 °C). XRD patterns of the Pd/Ga products revealed only broad diffraction peaks corresponding to orthorhombic Pd_2Ga (Figure 1a); no other crystalline phases such as Pd(0), Ga(0), Pd−Ga alloys, or oxidized phases were identified. More defined Pd_2Ga reflections are obtained on increasing the reduction temperature, indicating a slightly larger Pd_2Ga NP size (increasing from 4.6 to 5.7 nm). It is noteworthy that, in contrast to many intermetallic compounds that exhibit precisely defined stoichiometry, the Pd_2Ga phase can exist over a relatively broad compositional range and should more correctly be referred to as $Pd_{2+x}Ga_{1-x}$.[47,48] In good agreement with the XRD characterization, HR-TEM analyses of the Pd/Ga colloids show the presence of well-defined spherical NPs with a lattice spacing consistent with the Pd_2Ga crystalline phase (Figure 2).

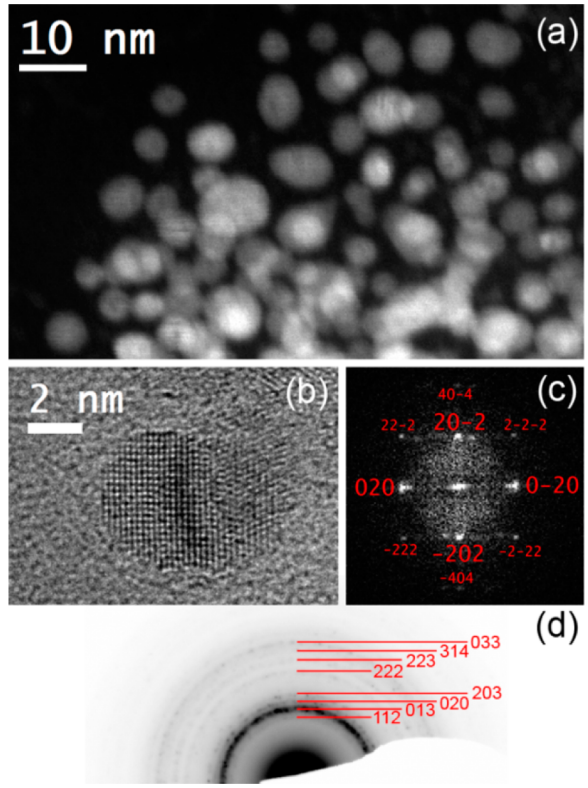

Figure 2. TEM analysis of the reduced Pd/Ga samples (PdGa290/2:1) showing the formation of Pd_2Ga NPs: (a) representative ADF STEM image; (b) HR-TEM image of an individual Pd_2Ga NP; (c) Fourier transform of (b) with reflections indexed by their respective {*hkl*} indices; (d) electron diffraction pattern from many nanoparticles. Rings are labeled with corresponding {*hkl*} families for Pd_2Ga.

No other crystalline phases were ever observed, despite the analysis of numerous high-resolution images. Table 1 shows the average size of the Pd_2Ga NPs, which slightly increases with the reduction temperature, from 4.8 to 5.8 nm. The increase can be partially attributed to an increase in volume upon incorporation of Ga into Pd to form the alloy, which is estimated to be 48% (14% in radius), or to some ripening at higher reduction temperatures.

The results indicate that the gallium stearate can be reduced to form a Ga(0) alloy at temperatures as low as 210 °C. It is important to note that no Ga(0)-containing phase was formed without the presence of Pd, as revealed by control experiments (see section 3.2, sample PdGa290/0:1). The role of the palladium can be understood by considering its ability to activate hydrogen, either by forming active hydrides or through hydrogen dissociation,[30,49] which mediates the reduction of gallium.[50] It is, therefore, proposed that the Ga(III) reduction

DOI: 10.1021/acscatal.6b02928
ACS Catal. 2017, 7, 1186−1196

Table 1. Average Particle Size for the Pd/Ga Colloids and Ga_{Ga2O3}/Ga_{Pd2Ga} Molar Ratio Determined by TEM and XPS, Respectively

sample	av particle size (nm)[a] (standard deviation)	Ga_{Ga2O3}/Ga_{Pd2Ga}[b] Ga $2p_{3/2}$	Ga $3d$
PdGa290/1:0	5.0 ± 0.1 (1.1)		
PdGa210/2:1	4.8 ± 0.1 (1.4)	1.27	0.61
PdGa250/2:1	5.8 ± 0.1 (1.8)		
PdGa290/3:1	5.8 ± 0.1 (1.6)	0.79	0.19
PdGa290/2:1	5.6 ± 0.1 (1.7)	1.00	0.78
PdGa290/1:1	5.5 ± 0.1 (1.5)	1.63	1.00
PdGa290/1:2	5.7 ± 0.1 (1.3)	2.03	1.38

[a]Average particle size and standard error were determined by TEM. The standard error of the mean is defined as standard deviation/(no. of measures)$^{1/2}$. [b]Molar ratio of the Ga forming Ga_2O_3 and the Pd_2Ga alloy determined by XPS at different core levels.

only occurs on the surface of the Pd(0) NPs, after which Ga(0) species can diffuse into the Pd(0) core to form the Pd_2Ga alloy. It should also be considered that the Pd-mediated reduction of $Ga(OSt)_3$, or its thermal decomposition at ~250 °C (Figure S2 in the Supporting Information), likely leads to the formation of stearic acid in the reaction medium, which may itself undergo reduction, in the presence of H_2 and high temperatures, to octadecanol.[9,13] Both species have been reported to effectively stabilize colloidal NPs.[9,13,51] Given the thermal decomposition of the precursors at 290 °C, and the lack of any other phases or byproducts observed, it is likely that the yield is quantitative; however, due to the difficulties in isolating the product from squalane, an absolute mass yield could not be obtained.

The surfaces of samples at each stage of preparation were also characterized by XPS. In order to analyze the XPS spectra of the sample $PdGa190N_2$, a pure metallic Pd reference sample was prepared, applying the described preparation method using the strongest reduction temperature of 290 °C (PdGa290/1:0). The formation of the elemental Pd crystalline phase for the PdGa290/1:0 sample was confirmed by XRD and TEM (vide infra). The Pd $3d$ core level spectrum for $PdGa190N_2$ (Figure 3a) exhibits two contributions: one at the binding energy position of Pd(0) (335.2 eV) and one at a higher binding energy typical for a Pd−Ga environment (335.7 eV). Some asymmetry from the metallic Pd is still visible in the Pd $3d$ core level; however, the metallic character of the Pd is much more evident in the valence band (VB) spectra (Figure 3b). In the purely metallic Pd sample, PdGa290/1:0, a high density of states is found at the Fermi energy E_F, stemming from Pd 4d states.[30] Covalent interaction of Pd with, for example, Ga can lead to a shift of the Pd 4d band maximum away from E_F, which

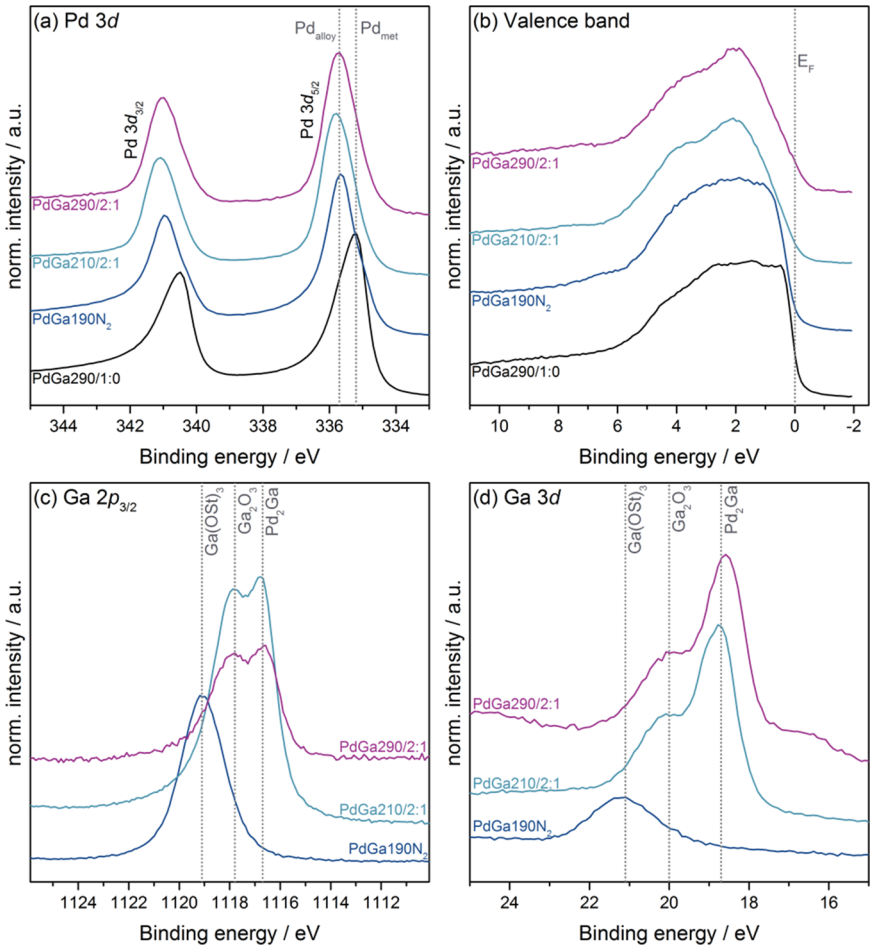

Figure 3. XPS spectra for Pd/Ga samples at different preparation steps and reduction temperatures, including (a) Pd $3d$ core level, (b) valence band spectrum, (c) Ga $2p_{3/2}$ core level, and (d) Ga $3d$ core level. Parts (a) and (b) also include spectra for the pure Pd sample (PdGa290/1:0) as reference. All spectra were normalized to the Pd $3d_{5/2}$ peak.

DOI: 10.1021/acscatal.6b02928
ACS Catal. 2017, 7, 1186−1196

in turn also leads to the loss of asymmetry in the Pd 3*d* core level.[52] The valence band of PdGa190N$_2$ still shows predominantly Pd(0) character, although a small shift away from E_F is already noticeable. There is clear evidence in both Pd 3*d* and VB spectra for the formation of metallic Pd, in accordance with XRD characterization. To understand whether Pd_2Ga is already formed, at this stage, one has to consider the Ga core levels shown in Figure 3c,d. Both show one high binding energy feature typical for the precursor $Ga(OSt)_3$ at 1119.1 eV (Ga $2p_{3/2}$) and one at 21.1 eV (Ga 3*d*). No additional peaks toward lower binding energy are observed, which excludes the formation of Pd_2Ga at this stage.

Pd/Ga samples reduced at 210 and 290 °C show a symmetric Pd 3*d* core level typical of an alloy phase with the Pd $3d_{5/2}$ line at a binding energy of 335.8 eV. This position agrees well with the values previously reported for Pd_2Ga in the literature,[30,52,53] as well as with the XRD and TEM characterization. The asymmetry characteristic for metallic Pd(0) has been completely lost, and its absence is further confirmed by the strong shift at the top of the valence band away from the Fermi energy E_F. When the Ga $2p_{3/2}$ and Ga 3*d* core levels are compared, it is evident that both comprise two resolved components with differences in BE of 1.1 and 1.3 eV, respectively, with varying relative intensities (Figure 3c,d). These features are consistent with Ga species forming Pd_2Ga and Ga_2O_3 and will be discussed in more detail later. Furthermore, the Ga $2p_{3/2}$ peak in particular shows some tailing on its higher BE side, most probably due to the presence of residual $Ga(OSt)_3$.

3.2. Influence of the Pd/Ga Composition. A series of colloidal Pd/Ga catalysts were prepared, using the method described, at different molar ratios of the $Pd(OAc)_2$ and $Ga(OSt)_3$ precursors, while the overall loading of metals was kept constant, and at a reduction temperature of 290 °C, which favors the formation of the Pd_2Ga alloy. The XRD patterns (Figure 1b) show that, with the use of only $Pd(OAc)_2$, the sample PdGa290/1:0 produces pure crystalline Pd(0) NPs, with an average crystallite size of 4.6 nm. The use of a Pd:Ga molar ratio of 3:1 yields a product featuring the reflections due to the Pd_2Ga crystalline phase with a pronounced shoulder at 39.9° (111) related to the pure Pd(0) phase, which is ascribed to the nominal Pd remaining unalloyed. When the Pd:Ga molar ratio was decreased to 2:1, and lower, only Pd_2Ga diffractions were observed. Interestingly, even using an excess of Ga (relative to the amount required for the Pd_2Ga alloy), no other Ga-containing crystalline phases were observed (samples PdGa290/1:1 and PdGa290/1:2); any Ga-rich phase must be amorphous. The use of a Pd:Ga ratio lower than 2:1 reduces the definition of the characteristic Pd_2Ga diffractions, an effect that might be attributed to dilution by an amorphous Ga-containing phase.

TEM characterization showed the presence of spherical NPs, whose electron diffraction patterns confirmed the formation of the Pd_2Ga phase for the Pd/Ga samples (Figure 4), while metallic Pd(0) was identified for the sample in absence of Ga, PdGa290/1:0 (Figure S4 in the Supporting Information). The slightly larger average size of the Pd_2Ga NPs, ~5.6 nm, compared to the pure Pd(0) sample, 5.0 nm, can be attributed to an increase in volume on forming the alloy. The samples with Pd:Ga ratio lower than 2 (PdGa290/1:1, PdGa290/1:2) contained an amorphous phase covering the Pd_2Ga NPs (Figure 4a). EDX map analysis indicated a high concentration of Ga and oxygen species where this amorphous phase was

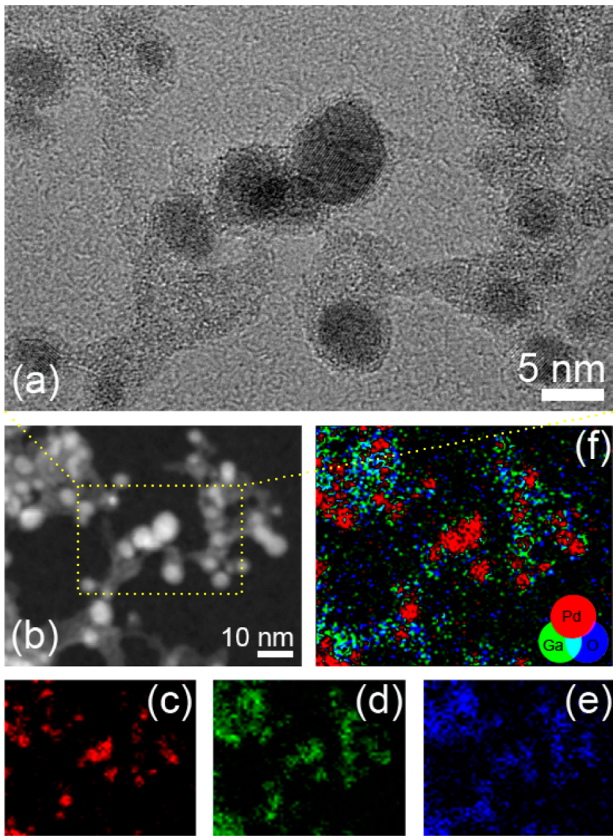

Figure 4. (a) TEM and (b) ADF-STEM representative images of the sample PdGa290/1:1 showing the presence of Pd_2Ga NPs covered by and amorphous Ga_2O_3 phase. (c–e) EDX maps of Pd (red), Ga (green), and O (blue) of the region in b. (f) Composite image formed by adding images (d) and (e) and superimposing (c). When the image is displayed in this way, red shows the location of the Pd_2Ga nanoparticles, and blue/green shows the location of Ga_2O_3.

located, indicating the formation of a Ga_2O_3 phase on the surface of the Pd_2Ga NPs.

XPS (Figure 5a,b) shows a striking difference between the mixed Pd/Ga samples and the pure Pd sample (PdGa290/1:0). As discussed previously, the Pd 3*d* core level and corresponding valence band spectrum of PdGa290/1:0 show the characteristic features of metallic Pd, including the BE position (335.2 eV) and a strong asymmetry of the core line shape, which is directly related to a large density of states at the Fermi energy E_F from Pd 4d states. While the VB of Pd_2Ga is still dominated by Pd 4d states with only a slight influence from the Ga 4s and 4p states, the Pd 4d maximum shifts away from E_F. A nonzero intensity at E_F remains in Pd_2Ga and leads to a metal-type behavior of this alloy. The low-intensity features below the main valence band of Pd_2Ga are due to Pd 5s and Ga 4s states.[54] The Pd $3d_{5/2}$ core level maximum of the mixed Pd/Ga samples lies at 335.6 eV, which is in accordance with previously reported values for the formation of the Pd_2Ga alloy.[30,52,53]

As mentioned above, the Ga 2*p* and 3*d* core lines consist of two resolved components (Figure 5c,d). Their average BE positions are 1116.6 and 1117.9 eV in Ga $2p_{3/2}$ and 18.6 and 20.0 eV in Ga 3*d*, with an average variation of 0.3 eV around these values. The lower BE component agrees well with literature data for Pd_2Ga,[30,52,53,55] while the higher BE feature corresponds to Ga_2O_3.[56−58] The relative ratios of these two components vary between samples but also between the two

DOI: 10.1021/acscatal.6b02928
ACS Catal. 2017, 7, 1186−1196

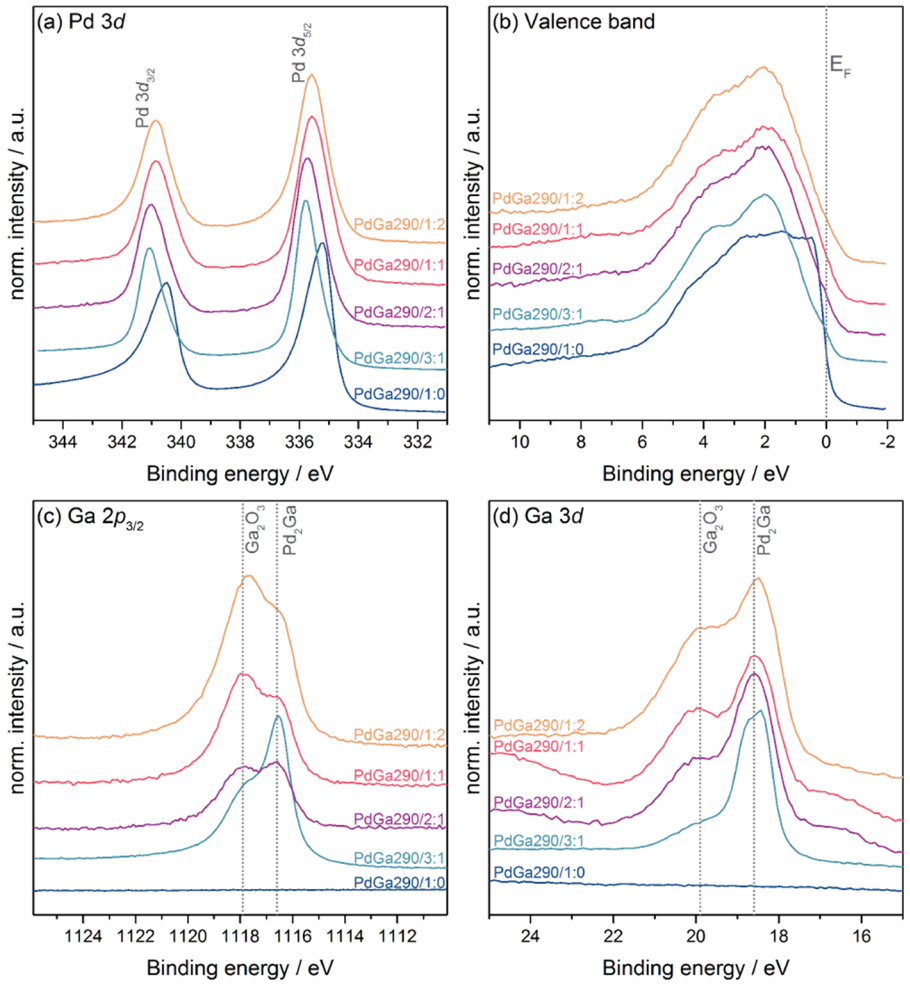

Figure 5. XPS spectra for Pd/Ga samples with different Pd/Ga ratios, including (a) Pd 3*d* core level, (b) valence band spectrum, (c) Ga $2p_{3/2}$ core level, and (d) Ga 3*d* core level. All spectra were normalized to the Pd $3d_{5/2}$ peak.

core levels. The variation between Ga 2*p* and 3*d* stems from a large difference in the kinetic energy E_K of the photoelectrons, with ΔE_K being on the order of 1 keV. The surface sensitivity of the two signals is starkly different, with the lower energy Ga 2*p* being a great deal more surface sensitive than Ga 3*d*. Using the approach by Tanuma, Powell, and Penn (TPP-2M method), the inelastic electron mean free path (IMFP) can be calculated, which is a good measure for the depth sensitivity of certain core levels.[43] As a close approximation, the IMFP values were correlated for gallium at the average binding energies of the Ga $2p_{3/2}$ and Ga 3*d* core levels, 1117 and 19 eV, respectively. Calculations on the basis of these values result in an approximately 3 times higher IMFP for Ga 3*d*, with the exact values being 11.28 Å for Ga $2p_{3/2}$ and 31.07 Å for Ga 3*d*. As the intensity of the Ga_2O_3 component is comparatively larger in the Ga 2*p* than in the Ga 3*d* core level, it can be concluded that the Ga_2O_3 is predominantly located on the surface of the Pd_2Ga NPs. When samples prepared with different Pd:Ga ratios are compared, the sample containing insufficient Ga to form the Pd_2Ga alloy (PdGa290/3:1) is the only one to show a small proportion of Ga oxide in comparison to Pd_2Ga regardless of surface sensitivity. From peak fits to the Ga $2p_{3/2}$ and 3*d* core levels, atomic ratios of the two Ga-containing phases, Pd_2Ga and Ga_2O_3, were calculated (Table 1). The Ga_{Ga2O3}/Ga_{Pd2Ga} molar ratio increases with the relative amount of Ga in the sample. Furthermore, on comparison of the Ga_{Ga2O3}/Ga_{Pd2Ga} values for the same sample, it can also be clearly seen that the Ga_2O_3 is more predominant in the lower energy Ga$2p_{3/2}$ spectra, in accordance with the differences in surface sensitivity discussed above.

The characterization results point to the formation of an amorphous Ga_2O_3 phase on the surface of the Pd_2Ga NPs, which is more prominent with increasing Ga content. The formation of this phase can be mostly attributed to the thermal decomposition of the $Ga(OSt)_3$ precursor during the reduction step. A control experiment treating $Ga(OSt)_3$ under the same conditions (reduction at 290 °C) revealed only the feature at 1117.9 eV at the Ga $2p_{3/2}$ position assigned to the Ga_2O_3 phase (Figure S5 in the Supporting Information). Furthermore, the XRD spectrum showed no crystalline diffraction features, confirming the amorphous nature of the Ga_2O_3 phase (Figure S6 in the Supporting Information). Therefore, it is reasonable to infer that the use of excess of $Ga(OSt)_3$ to form the Pd_2Ga alloy will evolve into the Ga_2O_3 phase. However, it is also possible that some Ga species are not fully incorporated into the Pd_2Ga alloy, particularly when stoichiometric or sub-stoichiometric Pd:Ga ratios are used, leading to the continued formation of a low concentration of the Ga_2O_3 phase. In fact, even the Ga-deficient PdGa290/3:1 sample exhibited weak Ga_2O_3 features in the XPS (Figure 5). Other routes may explain the Ga_2O_3 formation for this Pd-rich sample. For instance, adventitious trace oxidants in the precursors, solvent, or

DOI: 10.1021/acscatal.6b02928
ACS Catal. 2017, 7, 1186−1196

atmosphere used during the synthesis or for characterization may come into contact with the Pd_2Ga NPs. The Pd_2Ga surface has recently been reported to be unstable to traces of oxidizing agents, leading to Ga segregation and oxidation on the surface to form a GaO_x layer;[30,47,52] a pure intermetallic surface can only be achieved under highly reducing atmospheres.[52]

3.3. Catalytic Experiments. *3.3.1. Influence of the Reduction Temperature.* It was important to understand the relationship between the catalyst reduction temperature, applied during synthesis, and catalytic behavior. Therefore, samples with Pd:Ga molar ratios of 2:1 were reduced at different temperatures (210, 250, and 290 °C), and the products were tested in the hydrogenation of CO_2 to methanol. The only byproduct identified was CO, which comes from the well-known parasitic reverse water-gas shift reaction (rWGSR). As shown in Figure 6, the methanol synthesis rate normalized

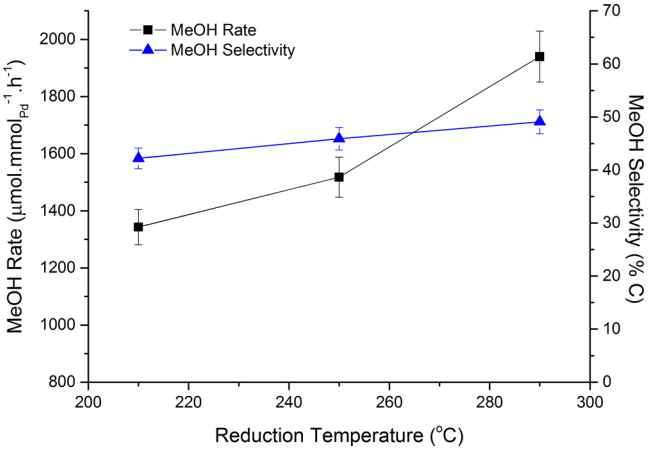

Figure 6. Methanol rate and selectivity for the colloidal PdGa*x*/2:1 catalysts reduced at 210, 250, and 290 °C. Reaction conditions: 210 °C, 5.0 MPa, GHSV = 18.9 L $mmol_{PdGa}^{-1}$ h^{-1}, and CO_2/H_2 = 3/1.

according to the amount of Pd present clearly increases with the reduction temperature. Since an increased reduction temperature mostly promotes the decomposition of the $Ga(OSt)_3$ precursor and the formation of the Pd_2Ga alloy from the initial Pd(0) phase, as discussed, the result underscores the importance of the Pd_2Ga phase as the active catalyst for the methanol synthesis.[24,39] Indeed, catalysts based only on metallic Pd(0) NPs (with similar particle sizes) or using only Ga_2O_3 showed no activity for either methanol synthesis or the rWGSR. For the active catalysts, increased reduction temperature leads to a slight enhancement in MeOH selectivity from ca. 45 to 50%, which suggests a high activity toward the rWGSR. Although some authors have attributed the CO formation to unalloyed Pd(0),[34] we found that metallic Pd alone is barely active toward the rWGSR, which is in accord with some other studies.[23] Here, the data indicate that the rWGSR active sites are related to the Pd_2Ga alloy.

The results highlight the need to form the Pd_2Ga alloy to obtain active catalysts for the methanol synthesis from CO_2; however, XPS also showed the existence of Ga_2O_3 species on the surface of the Pd_2Ga NPs, which may influence catalytic activity, as will be discussed in more detail in the following section.

3.3.2. Influence of Pd/Ga Composition. A series of colloidal Pd/Ga catalysts with variable Pd:Ga ratios (but all reduced at the optimum temperature of 290 °C) were compared in the

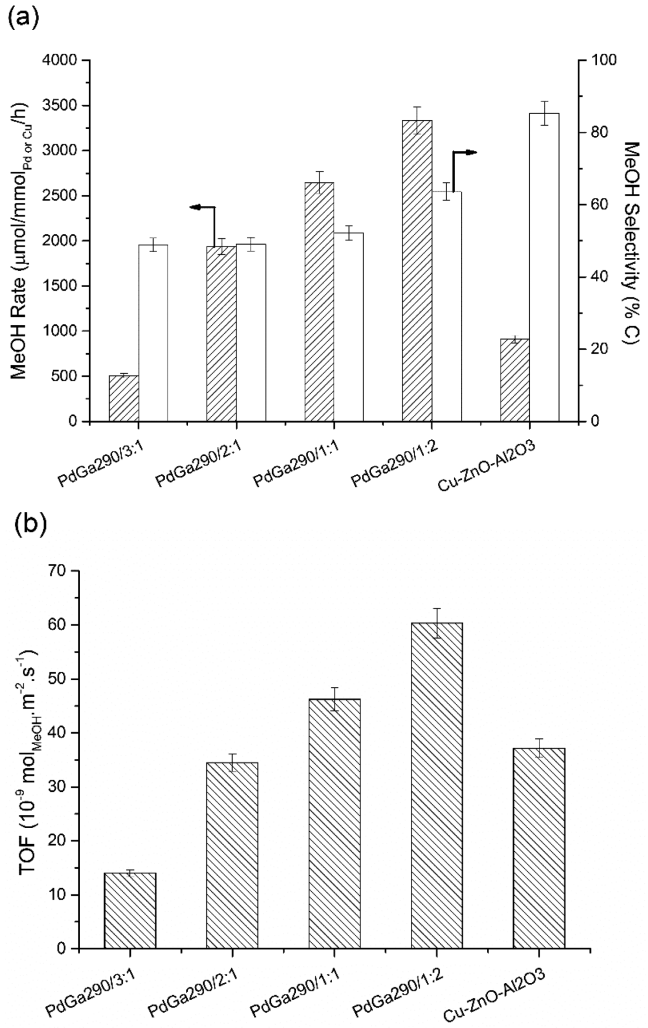

Figure 7. (a) Methanol synthesis rate and selectivity for the colloidal Pd/Ga catalysts with varying Pd:Ga molar ratio and (b) their corresponding turnover frecuencies (TOF) measured as $mmol_{CH3OH}$ m^{-2} s^{-1}. The commercial Cu-ZnO-Al_2O_3 is included as a reference. Reaction conditions: 210 °C, 5.0 MPa, GHSV = 18.9 L $mmol_{metal}^{-1}$ h^{-1}, and CO_2/H_2 = 3/1.

methanol synthesis reaction. Furthermore, the commercial Cu-ZnO-Al_2O_3 catalyst was also included as a benchmark. The methanol synthesis rate (Figure 7a) increases gradually with Ga content in the catalyst, reaching the highest value at a Pd:Ga molar ratio of 1:2. Remarkably, the methanol synthesis activity for this PdGa290/1:2 catalyst is nearly 4-fold higher than that obtained for the benchmark Cu-ZnO-Al_2O_3, when it is normalized for the content of Pd or Cu. On the other hand, considering the activity per total molar metal (Pd + Ga) content, the PdGa290/1:1 (and PdGa290/2:1) catalyst exhibited the maximum performance (Figure S7 in the Supporting Information). While a direct comparison with the current colloidal system is difficult, similar activity improvements have been observed for some fully heterogeneous, fixed-bed systems, with 2-fold[23] and 5-fold[24] increases reported for heterogeneous Pd/Ga_2O_3 catalysts relative to the conventional Cu-ZnO-Al_2O_3, normalized by mass of catalyst and Pd/Cu content, respectively. Other previous heterogeneous catalysts have shown a similar or reduced activity in comparison to the Cu-ZnO-Al_2O_3 benchmark[32,34]»

DOI: 10.1021/acscatal.6b02928
ACS Catal. 2017, 7, 1186−1196

In parallel with the activity trend, the MeOH selectivity was also moderately enhanced with a reduction in Pd:Ga ratio from 49% (PdGa290/2:1) to 64% (PdGa290/1:2), though the values are still lower than that for the reference catalyst (85%). MeOH selectivity values are in the range reported for heterogeneous catalysts based on supported Pd_2Ga NPs, suggesting a similar catalytic behavior.[23,24,27,34,39]

On the basis of the average particle size and with the assumption of spherical metal particles, turnover frequencies (TOFs) can be estimated, for the methanol production rate, as $mol_{CH3OH}\ m^{-2}\ s^{-1}$. For the Pd/Ga samples, the average Pd_2Ga particle size was obtained by TEM. For the reference Cu-ZnO-Al_2O_3 catalyst, the methanol rate is generally correlated to the initial Cu(0) surface area.[4,59] Therefore, the TOF was estimated from the average Cu(0) particle size after activation (6.3 nm, Figure S8 in the Supporting Information). In this case, Scherrer analysis of the XRD data was used for the size estimate due to agglomeration of the heterogeneous Cu-ZnO-Al_2O_3 catalyst[39] hampering TEM image analysis. Nevertheless, the difference between the particle sizes estimated by XRD and HR-TEM appears to be lower than 10%. As seen in Figure 7b, the TOF increased prominently with a reduction in the Pd:Ga ratio. It is noteworthy that the TOF obtained for the PdGa290/1:2 catalyst was approximately 2-fold higher than that for the reference Cu-ZnO-Al_2O_3, revealing its higher intrinsic activity toward the methanol synthesis, in agreement with results obtained for heterogeneous catalysts.[24,39]

On the basis of the effects of varying the Pd:Ga ratio, it seems that the Ga_2O_3 phase identified on the surface of the Pd_2Ga NPs plays a crucial role in the catalysis. In fact, there is a strong linear correlation (Figure 8) between the intrinsic activity and the Ga_{Ga2O3}/Ga_{Pd2Ga} molar ratio determined by XPS. These results strongly suggest that both Pd_2Ga and Ga_2O_3 phases are involved in the formation of the methanol synthesis active sites. Although the specific mechanism taking place is beyond the scope of this study, the findings are in accordance with the mechanism recently suggested by Collins et al. for heterogeneous Pd/Ga_2O_3 catalysts, where the bimetallic Pd–Ga and the Ga_2O_3 phases provide different functions.[27,60,61] The proposed reaction pathway invokes the formation of bi(carbonates), generated by CO_2 adsorption on Ga_2O_3 surface sites, which are successively hydrogenated to formates, methylenebisoxy and methoxy species, and finally methanol. The ability of Ga_2O_3 to dissociate and chemisorb H_2 to give Ga–H species, which are able to adsorb CO_2 and hydrogenate the resulting carbonate groups, has been studied by concentration-modulation excitation spectroscopy (MES) in combination with phase-sensitive detection (PDS) experiments.[60] The Pd–Ga bimetallic crystallites are proposed to provide atomic hydrogen, via spillover, so as to hydrogenate or increase the concentration of carbonaceous intermediates bonded to Ga_2O_3.[27,60,61]

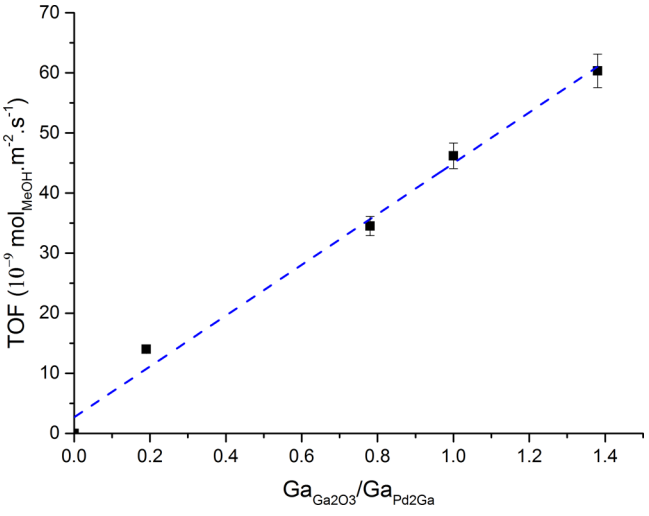

Figure 8. Turnover frequency (TOF) for the methanol synthesis versus the Ga_{Ga2O3}/Ga_{Pd2Ga} ratio determined by XPS from the Ga 3*d* core level for the Pd/Ga catalysts with different Pd:Ga compositions.

3.3.3. Influence of the Catalysis Conditions. Further methanol synthesis experiments were conducted using the optimized PdGa290/1:1 catalyst, which revealed the highest activity per millimole of metal (Pd + Ga), and the reference Cu-ZnO-Al_2O_3 catalyst at 190 and 240 °C with the aim of exploring the influence of the reaction temperature. As seen in Figure 9a, the methanol synthesis rate was clearly higher for the Pd/Ga catalyst in comparison to Cu-ZnO-Al_2O_3 across the temperature range studied, albeit with a lower methanol

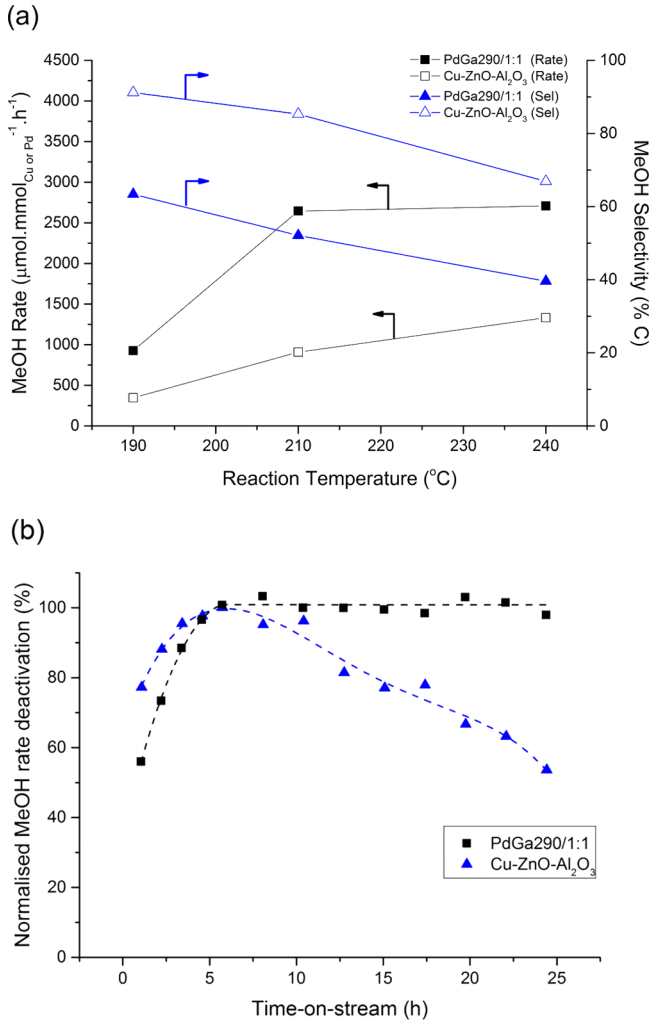

Figure 9. (a) Methanol rate and selectivity for the optimum PdGa290/1:1 and reference Cu-ZnO-Al_2O_3 catalysts performed at 190, 210, and 240 °C and (b) stability for 25 h time on stream at the reaction temperature of 210 °C. Reaction conditions: 5.0 MPa, GHSV = 18.9 L $mmol_{PdGa}^{-1}\ h^{-1}$, and CO_2/H_2 = 3/1.

DOI: 10.1021/acscatal.6b02928
ACS Catal. 2017, 7, 1186–1196

selectivity. As expected, an enhanced activity and decreased methanol selectivity with an increase in reaction temperature was found for both catalytic systems. However, the methanol rate trends significantly differ depending on the catalyst used. The methanol rate of the Cu-ZnO-Al_2O_3 catalyst gradually rises over the whole range of temperature. On the other hand, the Pd/Ga catalyst experiences a drastic increase in the methanol rate from 190 to 210 °C and then the rate remains nearly constant until 240 °C. This behavior might indicate a detrimental alteration of the methanol synthesis sites at the higher reaction temperature and identifies an optimum reaction temperature of 210 °C for the PdGa290/1:1 catalyst.

Finally, in order to assess the short-term stability, which is one of the main limitations of the commercial Cu-ZnO-Al_2O_3 catalysts when they are applied to methanol synthesis from CO_2,[8] the colloidal PdGa290/1:1 and the Cu-ZnO-Al_2O_3 catalysts were tested at the reaction temperature of 210 °C for 25 h. While the reference Cu-ZnO-Al_2O_3 exhibited a deactivation of ca. 50%, typically attributed to the sintering of the Cu and ZnO phases,[8,62] the Pd/Ga catalyst was completely stable over this time frame (Figure 9b). The postcatalysis mixture showed some black precipitate, indicating that the colloid might be partially agglomerated under the reaction conditions, but without affecting performance or reducing the effective active surface area. The postcatalysis XRD pattern did not show any significant changes, suggesting that the bulk of the Pd_2Ga phase is preserved, without ripening (Figure S9 in the Supporting Information). These findings were confirmed by TEM (Figure S10 in the Supporting Information), where Pd_2Ga NPs with an average size of 5.3 ± 0.1 nm were observed (before catalysis 5.5 ± 0.1 nm). The amorphous Ga_2O_3 phase was again observed to cover the NPs, and the catalyst generally appeared unchanged after reaction.

4. CONCLUSIONS

A simple methodology to prepare colloidal Pd/Ga catalysts for the liquid-phase production of methanol from CO_2 is described. The method, which involves the H_2 reduction of a mixture of $Pd(acetate)_2$ and $Ga(stearate)_3$ in a high-boiling-point solvent (squalane), is attractive, as it combines high performance with straightforward catalyst preparation. In the first step, palladium acetate is thermally decomposed, in the presence of the gallium stearate precursor, leading to the formation of Pd(0) nanoparticles of 3 nm size. Then, the palladium nanoparticles mediate the hydrogen reduction of Ga(III) species, at 210−290 °C, leading to the formation of Pd_2Ga nanoparticles with an average size of 5−6 nm. Interestingly, XPS analysis, exploiting the different surface sensitivity as a function of the kinetic energy of the emitted photoelectrons, showed the formation of a Ga_2O_3 phase located on the surface of the nanoparticles. The amount of this Ga_2O_3 phase was easily tuned by modifying the molar Pd:Ga ratio supplied by the precursors. Methanol synthesis experiments using the Pd_2Ga-based colloids indicated that a reduction temperature of 290 °C leads to the highest methanol synthesis activity, which is attributed to the formation of the Pd_2Ga phase. Furthermore, when the Ga_2O_3 content was increased, a dramatic increment in the intrinsic activity was obtained. These results point to a bifunctional active site where both the Pd_2Ga and Ga_2O_3 phases are implicated in methanol synthesis.

The optimum Pd/Ga catalyst was benchmarked against the commercial Cu-ZnO-Al_2O_3 using a reaction temperature range of 190−240 °C. The methanol synthesis activity for the Pd/Ga catalyst was higher than that obtained for the commercial catalyst based on Cu-ZnO-Al_2O_3, although the methanol selectivity was slightly lower, due to higher CO formation. An optimum activity was found at 210 °C, resulting in a 4-fold higher activity in comparison to that for the commercial catalysts (in terms of Pd or Cu molar content). Furthermore, short-term stability studies over 25 h time on stream revealed that the Cu-ZnO-Al_2O_3 catalyst underwent significant deactivation, in line with the literature results; however, in contrast, no deactivation was observed for the colloidal Pd/Ga catalyst. Additionally, characterization of the sample post-catalysis showed the retention of the nanoscale structure; these data indicate promising stability for the Pd/Ga colloidal catalysts. The new colloidal Pd_2Ga catalysts show significant promise in terms of activity, stability, and ability to operate at lower temperatures for the hydrogenation of CO_2 to methanol. It is expected that both the method of synthesis and the catalysts themselves should be more broadly applicable to a range of other reduction and catalytic processes and further development of such colloidal systems is warranted.

■ ASSOCIATED CONTENT

Supporting Information

The Supporting Information is available free of charge on the ACS Publications website at DOI: 10.1021/acscatal.6b02928.

Different characterization results (EA, FTIR, TGA, TEM, XPS, XRD) of the precursors, as-synthesized samples, and postcatalysis samples and catalytic results (PDF)

■ AUTHOR INFORMATION

Corresponding Authors

*E-mail for D.J.P.: d.payne@imperial.ac.uk.
*E-mail for M.S.P.S.: m.shaffer@imperial.ac.uk.
*E-mail for C.K.W.: charlotte.williams@chem.ox.ac.uk.

ORCID

Anna Regoutz: 0000-0002-3747-3763
Charlotte K. Williams: 0000-0002-0734-1575

Notes

The authors declare no competing financial interest.

■ ACKNOWLEDGMENTS

The EPSRC is acknowledged for funding (EP/H046380, EP/K035274/1, EP/M013839/1, EP/M028291/1). D.J.P. acknowledges support from the Royal Society (UF100105).

■ REFERENCES

(1) Kondratenko, E. V.; Mul, G.; Baltrusaitis, J.; Larrazábal, G. O.; Pérez-Ramírez, J. *Energy Environ. Sci.* **2013**, *6*, 3112−3135.
(2) Olah, G. A. *Angew. Chem., Int. Ed.* **2005**, *44*, 2636−2639.
(3) Palo, D. R.; Dagle, R. A.; Holladay, J. D. *Chem. Rev.* **2007**, *107*, 3992−4021.
(4) Baltes, C.; Vukojević, S.; Schüth, F. *J. Catal.* **2008**, *258*, 334−344.
(5) Chinchen, G.; Denny, P.; Parker, D.; Spencer, M.; Whan, D. *Appl. Catal.* **1987**, *30*, 333−338.
(6) Dutta, G.; Sokol, A. A.; Catlow, C. R. A.; Keal, T. W.; Sherwood, P. *ChemPhysChem* **2012**, *13*, 3453−3456.
(7) Jadhav, S. G.; Vaidya, P. D.; Bhanage, B. M.; Joshi, J. B. *Chem. Eng. Res. Des.* **2014**, *92*, 2557−2567.
(8) Martin, O.; Martín, A. J.; Mondelli, C.; Mitchell, S.; Segawa, T. F.; Hauert, R.; Drouilly, C.; Curulla-Ferré, D.; Pérez-Ramírez, J. *Angew. Chem., Int. Ed.* **2016**, *55*, 6261−6265.

DOI: 10.1021/acscatal.6b02928
ACS Catal. 2017, 7, 1186−1196

(9) Schimpf, S.; Rittermeier, A.; Zhang, X.; Li, Z.-A.; Spasova, M.; vandenBerg, M. W. E.; Farle, M.; Wang, Y.; Fischer, R. A.; Muhler, M. *ChemCatChem* **2010**, *2*, 214−222.
(10) Rittermeier, A.; Miao, S.; Schröter, M. K.; Zhang, X.; van den Berg, M. W.; Kundu, S.; Wang, Y.; Schimpf, S.; Löffler, E.; Fischer, R. A. *Phys. Chem. Chem. Phys.* **2009**, *11*, 8358−8366.
(11) Schröter, M. K.; Khodeir, L.; van den Berg, M. W.; Hikov, T.; Cokoja, M.; Miao, S.; Grünert, W.; Muhler, M.; Fischer, R. A. *Chem. Commun.* **2006**, 2498−2500.
(12) Sliem, M. A.; Turner, S.; Heeskens, D.; Kalidindi, S. B.; Van Tendeloo, G.; Muhler, M.; Fischer, R. A. *Phys. Chem. Chem. Phys.* **2012**, *14*, 8170−8178.
(13) Brown, N. J.; Weiner, J.; Hellgardt, K.; Shaffer, M. S. P.; Williams, C. K. *Chem. Commun.* **2013**, *49*, 11074−11076.
(14) Brown, N. J.; García-Trenco, A.; Weiner, J.; White, E. R.; Allinson, M.; Chen, Y.; Wells, P. P.; Gibson, E. K.; Hellgardt, K.; Shaffer, M. S. *ACS Catal.* **2015**, *5*, 2895−2902.
(15) García-Trenco, A.; White, E. R.; Shaffer, M. S. P.; Williams, C. K. *Catal. Sci. Technol.* **2016**, *6*, 4389−4397.
(16) Le Valant, A.; Comminges, C.; Tisseraud, C.; Canaff, C.; Pinard, L.; Pouilloux, Y. *J. Catal.* **2015**, *324*, 41−49.
(17) Tisseraud, C.; Comminges, C.; Belin, T.; Ahouari, H.; Soualah, A.; Pouilloux, Y.; Le Valant, A. *J. Catal.* **2015**, *330*, 533−544.
(18) Poels, E.; Brands, D. *Appl. Catal., A* **2000**, *191*, 83−96.
(19) Astruc, D.; Lu, F.; Aranzaes, J. R. *Angew. Chem., Int. Ed.* **2005**, *44*, 7852−7872.
(20) Lee, S.; Sardesai, A. *Top. Catal.* **2005**, *32*, 197−207.
(21) García-Trenco, A.; Martínez, A. *Catal. Today* **2013**, *215*, 152−161.
(22) Fan, L.; Fujimoto, K. *J. Catal.* **1994**, *150*, 217−220.
(23) Fujitani, T.; Saito, M.; Kanai, Y.; Watanabe, T.; Nakamura, J.; Uchijima, T. *Appl. Catal., A* **1995**, *125*, L199−L202.
(24) Li, L.; Zhang, B.; Kunkes, E.; Föttinger, K.; Armbrüster, M.; Su, D. S.; Wei, W.; Schlögl, R.; Behrens, M. *ChemCatChem* **2012**, *4*, 1764−1775.
(25) Collins, S. E.; Baltanás, M. A.; Fierro, J. L. G.; Bonivardi, A. L. *J. Catal.* **2002**, *211*, 252−264.
(26) Collins, S. E.; Baltanás, M. A.; Bonivardi, A. L. *J. Catal.* **2004**, *226*, 410−421.
(27) Collins, S. E.; Delgado, J. J.; Mira, C.; Calvino, J. J.; Bernal, S.; Chiavassa, D. L.; Baltanás, M. A.; Bonivardi, A. L. *J. Catal.* **2012**, *292*, 90−98.
(28) Iwasa, N.; Mayanagi, T.; Nomura, W.; Arai, M.; Takezawa, N. *Appl. Catal., A* **2003**, *248*, 153−160.
(29) Iwasa, N.; Mayanagi, T.; Ogawa, N.; Sakata, K.; Takezawa, N. *Catal. Lett.* **1998**, *54*, 119−123.
(30) Haghofer, A.; Föttinger, K.; Girgsdies, F.; Teschner, D.; Knop-Gericke, A.; Schlögl, R.; Rupprechter, G. *J. Catal.* **2012**, *286*, 13−21.
(31) Qu, J.; Zhou, X.; Xu, F.; Gong, X.-Q.; Tsang, S. C. E. *J. Phys. Chem. C* **2014**, *118*, 24452−24466.
(32) Zhou, X.; Qu, J.; Xu, F.; Hu, J.; Foord, J. S.; Zeng, Z.; Hong, X.; Tsang, S. C. E. *Chem. Commun.* **2013**, *49*, 1747−1749.
(33) Haghofer, A.; Ferri, D.; Föttinger, K.; Rupprechter, G. n. *ACS Catal.* **2012**, *2*, 2305−2315.
(34) Ota, A.; Kunkes, E. L.; Kasatkin, I.; Groppo, E.; Ferri, D.; Poceiro, B.; Yerga, R. M. N.; Behrens, M. *J. Catal.* **2012**, *293*, 27−38.
(35) Penner, S.; Lorenz, H.; Jochum, W.; Stoeger-Pollach, M.; Wang, D.; Rameshan, C.; Kloetzer, B. *Appl. Catal., A* **2009**, *358*, 193−202.
(36) Lorenz, H.; Penner, S.; Jochum, W.; Rameshan, C.; Kloetzer, B. *Appl. Catal., A* **2009**, *358*, 203−210.
(37) Chiavassa, D. L.; Barrandeguy, J.; Bonivardi, A. L.; Baltanas, M. A. *Catal. Today* **2008**, *133*−*135*, 780−786.
(38) Chiavassa, D. L.; Collins, S. E.; Bonivardi, A. L.; Baltanas, M. A. *Chem. Eng. J.* **2009**, *150*, 204−212.
(39) Fiordaliso, E. M.; Sharafutdinov, I.; Carvalho, H. W. P.; Grunwaldt, J.-D.; Hansen, T. W.; Chorkendorff, I.; Wagner, J. B.; Damsgaard, C. D. *ACS Catal.* **2015**, *5*, 5827−5836.
(40) Liang, X.; Ren, Y.; Bai, S.; Zhang, N.; Dai, X.; Wang, X.; He, H.; Jin, C.; Ye, Z.; Chen, Q.; Chen, L.; Wang, J.; Jin, Y. *Chem. Mater.* **2014**, *26*, 5169−5178.
(41) Chen, Y.; Johnson, E.; Peng, X. *J. Am. Chem. Soc.* **2007**, *129*, 10937−10947.
(42) Otero, V.; Sanches, D.; Montagner, C.; Vilarigues, M.; Carlyle, L.; Lopes, J. A.; Melo, M. J. *J. Raman Spectrosc.* **2014**, *45*, 1197−1206.
(43) Tanuma, S.; Powell, C. J.; Penn, D. R. *Surf. Interface Anal.* **1994**, *21*, 165−176.
(44) van der Laan, G. P.; Beenackers, A. A. C. M.; Ding, B.; Strikwerda, J. C. *Catal. Today* **1999**, *48*, 93−100.
(45) Sawant, A.; Ko, M. K.; Parameswaran, V.; Lee, S.; Kulik, C. J. *Fuel Sci. Technol. Int.* **1987**, *5*, 77−88.
(46) Teranishi, T.; Miyake, M. *Chem. Mater.* **1998**, *10*, 594−600.
(47) Leary, R.; de la Peña, F.; Barnard, J. S.; Luo, Y.; Armbrüster, M.; Meurig Thomas, J.; Midgley, P. A. *ChemCatChem* **2013**, *5*, 2599−2609.
(48) Wannek, C.; Harbrecht, B. *J. Alloys Compd.* **2001**, *316*, 99−106.
(49) Borodziński, A.; Janko, A. *React. Kinet. Catal. Lett.* **1977**, *7*, 163−169.
(50) Armbrüster, M.; Wowsnick, G.; Friedrich, M.; Heggen, M.; Cardoso-Gil, R. *J. Am. Chem. Soc.* **2011**, *133*, 9112−9118.
(51) Luo, S.; Feng, J.; Ng, K. M. *CrystEngComm* **2014**, *16*, 9236−9244.
(52) Wowsnick, G.; Teschner, D.; Kasatkin, I.; Girgsdies, F.; Armbrüster, M.; Zhang, A.; Grin, Y.; Schlögl, R.; Behrens, M. *J. Catal.* **2014**, *309*, 209−220.
(53) Rameshan, C.; Stadlmayr, W.; Penner, S.; Lorenz, H.; Mayr, L.; Hävecker, M.; Blume, R.; Rocha, T.; Teschner, D.; Knop-Gericke, A. *J. Catal.* **2012**, *290*, 126−137.
(54) Wencka, M.; Schwerin, J.; Klanjšek, M.; Krnel, M.; Vrtnik, S.; Koželj, P.; Jelen, A.; Kapun, G.; Jagličić, Z.; Sharafutdinov, I.; Chorkendorff, I.; Gille, P.; Dolinšek, J. *Intermetallics* **2015**, *67*, 35−46.
(55) Mayr, L.; Lorenz, H.; Armbruester, M.; Villaseca, S. A.; Luo, Y.; Cardoso, R.; Burkhardt, U.; Zemlyanov, D.; Haevecker, M.; Blume, R.; Knop-Gericke, A.; Kloetzer, B.; Penner, S. *J. Catal.* **2014**, *309*, 231−240.
(56) Schön, G. *J. Electron Spectrosc. Relat. Phenom.* **1973**, *2*, 75−86.
(57) Epp, J. M.; Dillard, J. G. *Chem. Mater.* **1989**, *1*, 325−330.
(58) Regoutz, A.; Egdell, R. G.; Morgan, D. J.; Palgrave, R. G.; Téllez, H.; Skinner, S. J.; Payne, D. J.; Watson, G. W.; Scanlon, D. O. *Appl. Surf. Sci.* **2015**, *349*, 970−982.
(59) Chinchen, G.; Waugh, K.; Whan, D. *Appl. Catal.* **1986**, *25*, 101−107.
(60) Aguirre, A.; Collins, S. E. *Catal. Today* **2013**, *205*, 34−40.
(61) Collins, S. E.; Chiavassa, D. L.; Bonivardi, A. L.; Baltanás, M. A. *Catal. Lett.* **2005**, *103*, 83−88.
(62) Twigg, M. V.; Spencer, M. S. *Top. Catal.* **2003**, *22*, 191−203.

DOI: 10.1021/acscatal.6b02928
ACS Catal. 2017, 7, 1186−1196